

Design, Fabrication and Analysis of Unbalanced MZIs for Group Index Extraction

Cameron Bass
edX Username: cameron_02

University of British Columbia
Department of Electrical and Computer Engineering

Introduction

Silicon photonics is a growing technology for fabricating and integrating optical components on a chip, enabling high-speed communication [1], data transfer [2], signal processing [3], and quantum information [4]. It uses CMOS-compatible fabrication processes that are standard in industry and offers a compact, low-energy platform relative to its electronic counterparts.

A fundamental and widely used component of a photonic circuit is the Mach-Zehnder Interferometer (MZI). The MZI controls the phase and amplitude of light by splitting and recombining input light beams. It can be used as a thermo-optic switch, PN depletion modulator, and sensing devices [5]. In this project, we design and simulate an unbalanced MZI to enable the extraction of the waveguide's group index from the free spectral range (FSR) observed in its transmission spectrum.

We will use a strip waveguide geometry with an industry-standard height of 220nm and width of 500nm. We simulate the waveguide's mode profiles and effective index using Lumerical MODE Solutions, then build a compact model to fit its dispersion properties. The full MZI circuit is simulated in MATLAB and Lumerical INTERCONNECT, allowing me to explore how variations in path length difference (ΔL) affect the FSR and how this relationship can be used to calculate the group index. The design is structured to align with fabrication constraints and will ultimately be tested experimentally, with measured spectra compared against simulated results to verify group index extraction.

Theory

Group Index

The group index n_g is a quantity that describes how a light pulse behaves in a medium. Similar to the effective index, which describes the phase velocity of individual frequency components, the group index describes the group velocity and corresponds to the

speed of the overall pulse envelope. This is given by

$$n_g(\lambda) = n_{\text{eff}} - \lambda \frac{dn_{\text{eff}}}{d\lambda} \quad (1)$$

where n_{eff} is the effective index. Equation 1 accounts for both material and waveguide dispersion by assuming the effective index changes with wavelength.

MZI Model

An MZI typically consists of two 50:50 splitters (e.g. Y-branches) connected by two waveguide arms. When light is put through the input port, it is equally split into two arms (e.g. waveguides), each accumulating a phase shift as it propagates. The two waves then recombine at the second beam splitter, where the beams will either have constructive or destructive phase interference. In this project, we will design unbalanced MZIs, where the two arms will have varying lengths ΔL . Figure 1 shows a diagram of an unbalanced MZI, with input field E_i and output field E_o . At the input before the first Y-branch, we begin with input intensity I_i and electric field E_i . The light is split equally into two branches, such that

$$I_{i1} = I_{i2} = \frac{I_i}{2} \quad (2)$$

and we have $I \propto |E|^2$, so the electric field in the upper and lower arm after the first Y branch is

$$E_{i1} = \frac{E_i}{\sqrt{2}} \quad \text{and} \quad E_{i2} = \frac{E_i}{\sqrt{2}}. \quad (3)$$

After the phase shifters, the electric fields in the upper and lower waveguides are

$$E_{o1} = \frac{E_i}{\sqrt{2}} e^{i\beta_1 L_1 - \frac{\alpha_1}{2} L_1} \quad \text{and} \quad E_{o2} = \frac{E_i}{\sqrt{2}} e^{i\beta_2 L_2 - \frac{\alpha_2}{2} L_2} \quad (4)$$

where $\beta_{1,2}$ is the propagation constant of the wave, and $\alpha_{1,2}$ is the power attenuation coefficient, which models the optical loss in the waveguide. The propagation constant describes how the phase of the light wave evolves with distance, and is given by $\beta_{1,2} = \frac{2\pi n_{\text{eff}1,2}}{\lambda}$, where λ is the wavelength. The electric fields E_{o1} and E_{o2} consequently recombine at the

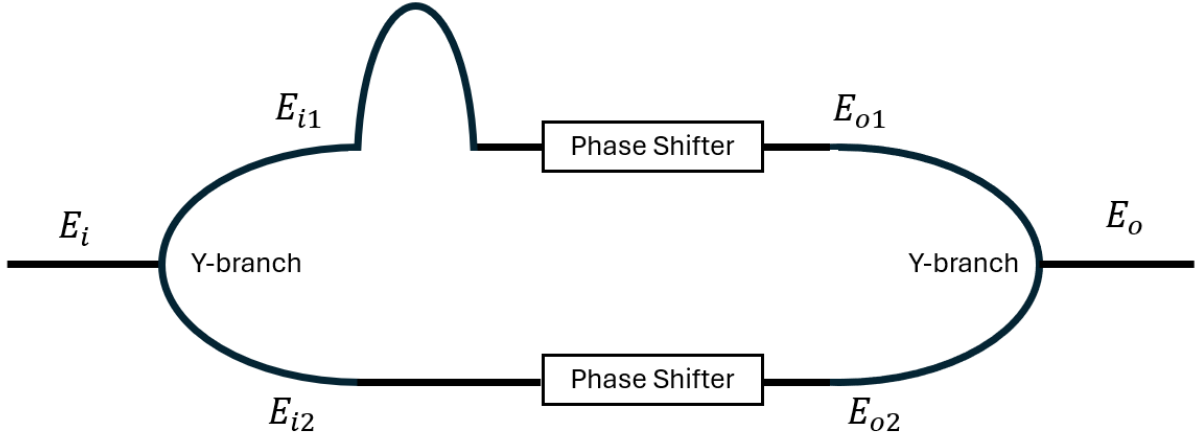


Figure 1: Schematic of an unbalanced Mach-Zehnder Interferometer (MZI) using Y-branches as splitters. The input electric field E_i is split equally into the two arms. The fields recombine at the second Y-branch, resulting in constructive or destructive interference at the output port E_o . This configuration enables wavelength-dependent transmission, allowing the extraction of the waveguide group index from the free spectral range (FSR).

second 50/50 beamsplitter (Y-branch) to produce a final output field

$$E_o = \frac{1}{\sqrt{2}}(E_{o1} + E_{o2}). \quad (5)$$

Substituting Equation 4 into 5, and using $I \propto |E|^2$, we have the output intensity

$$I_o = \frac{I_i}{4} |e^{i\beta_1 L_1 - \frac{\alpha_1}{2} L_1} + e^{i\beta_2 L_2 - \frac{\alpha_2}{2} L_2}|^2. \quad (6)$$

Assuming identical waveguides, we have $\beta_1 = \beta_2$, and setting $\alpha_1 = \alpha_2 = 0$ (lossless case), we can simplify Equation 6 to get

$$I_o = |E_o|^2 = \frac{I_i}{4} |1 + e^{-i\beta\Delta L}|^2. \quad (7)$$

Expanding the squared magnitude, we get the unbalanced MZI transfer function,

$$I_o = \frac{I_i}{2} [1 + \cos(\beta\Delta L)] \quad (8)$$

where $\Delta L = L_1 - L_2$. The output intensity of an unbalanced MZI oscillates sinusoidally with wavelength due to interference between light travelling through the two arms of different lengths. These oscillations form a periodic pattern in the transmission spectrum. The spacing between adjacent maxima (or minima) in the spectrum is known as the Free Spectral Range (FSR). The FSR represents the change in wavelength required to shift the phase difference between the arms by one full 2π . Starting from the MZI transfer function (Equation 8), we define the phase shift as:

$$\delta = \beta\Delta L$$

Constructive interference occurs when $\delta = 2\pi m$, for some integer m . The next constructive interference

occurs at $\lambda + \Delta\lambda$, where the phase shift increases by 2π :

$$\beta(\lambda + \Delta\lambda)\Delta L - \beta(\lambda)\Delta L = 2\pi \quad (9)$$

Using a first-order Taylor expansion, we approximate:

$$\Delta\beta \approx \frac{d\beta}{d\lambda} \cdot \Delta\lambda \quad (10)$$

Substituting into the phase condition:

$$\frac{d\beta}{d\lambda} \cdot \Delta\lambda \cdot \Delta L = 2\pi \quad (11)$$

Solving for $\Delta\lambda$, the FSR becomes:

$$\text{FSR} = \Delta\lambda = \frac{2\pi}{\Delta L \cdot \frac{d\beta}{d\lambda}} \quad (12)$$

Since $\beta = \frac{2\pi n}{\lambda}$, its derivative with respect to wavelength is:

$$\frac{d\beta}{d\lambda} = -\frac{2\pi}{\lambda^2} \left(n - \lambda \frac{dn}{d\lambda} \right) \quad (13)$$

Substituting into the FSR expression yields:

$$\text{FSR} = \frac{\lambda^2}{\Delta L \cdot n_g} \quad (14)$$

where the group index n_g is defined as:

$$n_g = n - \lambda \frac{dn}{d\lambda} \quad (15)$$

This result shows that the free spectral range is inversely proportional to both the path length difference ΔL and the group index n_g . By measuring the FSR from a simulated or experimental transmission spectrum and knowing the design value of ΔL , one can directly calculate the group index of the waveguide.

Modelling and Simulation

This model uses a strip waveguide width of 500nm and a height of 220 nm. The transfer function for the waveguide is given in Equation 8. Lumerical MODE solutions was used to simulate the electric field intensity of the TE and TM mode profiles, shown in Figure 2 and 3.

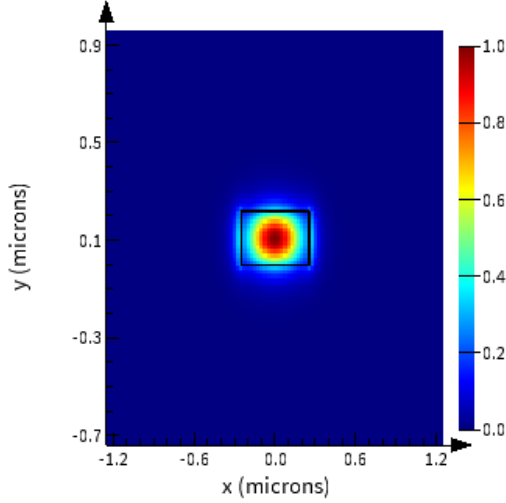


Figure 2: Electric field intensity of fundamental TE mode profile in waveguide, simulated in Lumerical MODE.

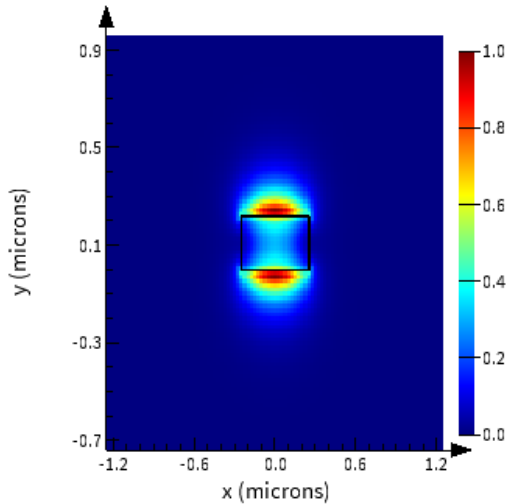


Figure 3: Electric field intensity of fundamental TM mode profile in waveguide, simulated in Lumerical MODE.

A wavelength sweep was performed between 1500 nm and 1600 nm to visualize both the effective and group indices. A plot of the effective index as a function of wavelength is shown in Figure 4.

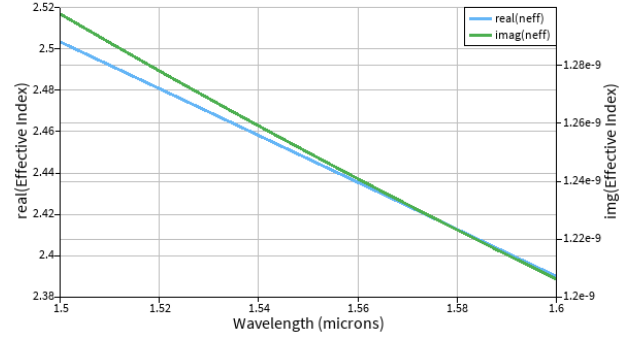


Figure 4: Effective index of the waveguide as a function of wavelength, simulated in Lumerical MODE.

We see n_{eff} increases with decreasing wavelength, which aligns with our expectations. As the wavelength decreases, the optical mode becomes more confined within the high-index silicon core, resulting in a larger effective index. We can also plot the group index as a function of wavelength, shown in Figure 5. Conversely, we see group index increases proportionally with wavelength.

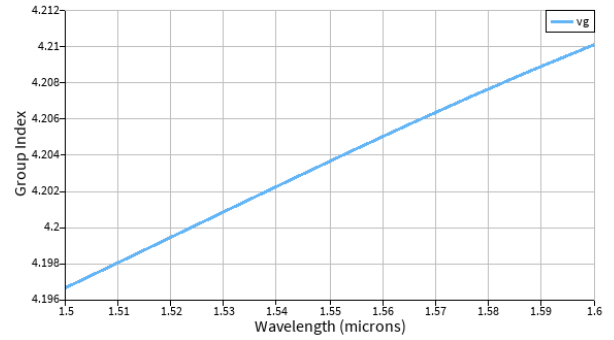


Figure 5: Group index of the waveguide as a function of wavelength, simulated in Lumerical MODE.

Through MATLAB, the waveguide model was fit to a second-order polynomial of the form

$$n_{\text{eff}}(\lambda) = n_1 + n_2(\lambda - \lambda_0) + n_3(\lambda - \lambda_0)^2 \quad (16)$$

where n_0, n_1, n_2 are polynomial coefficients. Due to waveguide dispersion, n_{eff} does not change at a constant rate with wavelength, so a second-order fit will provide a more accurate group index and FSR calculation. For the waveguide in this report, the complete compact model is given by

$$n_{\text{eff}}(\lambda) = 2.44 - 1.13(\lambda - \lambda_0) - 0.04(\lambda - \lambda_0)^2. \quad (17)$$

The preceding results for waveguide simulation were used to create an MZI model through Lumerical INTERCONNECT. Simulations were performed to calculate FSR values for various ΔL configurations, shown in Table 1.

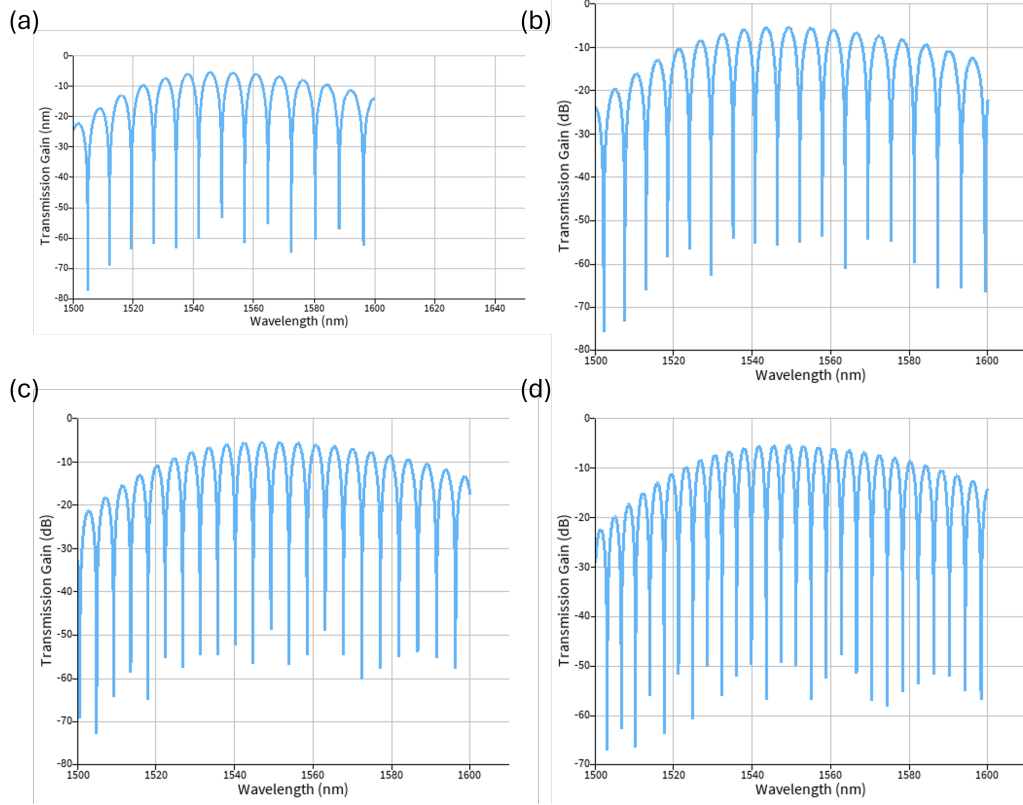


Figure 6: Transmission gain spectrum of imbalanced MZI for (a) 75 μm , (b) 100 μm , (c) 125 μm , (d) 150 μm , simulated through Lumerical INTERCONNECT.

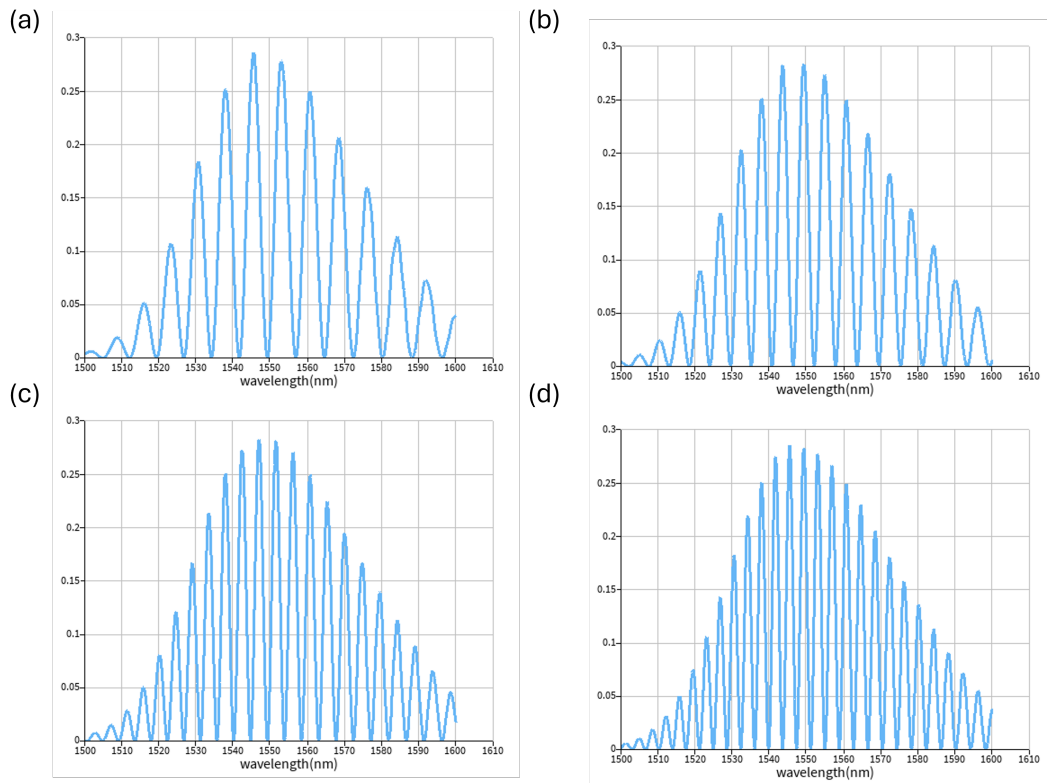


Figure 7: TE Transmission spectrum ($|Re|^2$) of imbalanced MZI for (a) 75 μm , (b) 100 μm , (c) 125 μm , (d) 150 μm , simulated through Lumerical INTERCONNECT.

ΔL (μm)	Simulated FSR (nm)
25	21.24
50	11.61
75	7.55
100	5.71
125	4.58
150	3.80

Table 1: Various FSR values for different MZI waveguide length separation

Corner	Width (nm)	Height (nm)
0 (Nominal)	500	220
1	470	215.3
2	470	223.1
3	510	215.3
4	510	223.1

Table 2: Corner values for waveguides with process variations

Additionally, transmission functions of the MZI were plotted for various ΔL values, shown in Figure 6. We observe as ΔL increases, FSR decreases. This is because a greater path length variation results in the interferometer accumulating a phase difference faster, producing more closely spaced interference fringes. Corresponding TE transmission spectra for each of the ΔL values in Table 1 are given in Figure 7.

Manufacturing Challenges

To consider how manufacturing challenges will affect the device, we can perform corner analysis on the waveguides used in the MZI. In this analysis, we assume that the waveguide cross-section is nominally $500 \text{ nm} \times 220 \text{ nm}$, with process variations spanning widths from 470 nm to 510 nm and thicknesses from 215.3 nm to 223.1 nm . These corners are summarized from 1-4 in Table 2.

Scripts in Lumerical MODE were used to simulate the group and effective index of waveguides with the aforementioned process variations. These values are shown in Table 3.

Corner	Group index (n_g)	n_{eff}
0 (Nominal)	4.191	2.436
1	4.22	2.36
2	4.24	2.40
3	4.15	2.43
4	4.17	2.46

Table 3: Group and effective index values for corners, at 1550 nm .

To accurately model the waveguide behaviour across a range of wavelengths, a compact model was generated for each corner. Using Lumerical MODE, a frequency sweep was performed around the central wavelength $\lambda_0 = 1550 \text{ nm}$, and the resulting effective index values were fitted to a second-order polynomial. This process differed slightly from Equation 17, instead utilizing Lumerical MODE scripts. The compact model captures dispersion effects and provides a smooth, differentiable representation of waveguide behavior needed for accurate Mach-Zehnder Interferometer (MZI) transfer function predictions. Equations 18-21 show the compact model of the process variation waveguides for corners 1-4:

$$n_{\text{eff}}(\lambda) = 2.36 - 1.19(\lambda - \lambda_0) - 0.021(\lambda - \lambda_0)^2, \quad (18)$$

$$n_{\text{eff}}(\lambda) = 2.40 - 1.18(\lambda - \lambda_0) - 0.041(\lambda - \lambda_0)^2, \quad (19)$$

$$n_{\text{eff}}(\lambda) = 2.43 - 1.10(\lambda - \lambda_0) - 0.023(\lambda - \lambda_0)^2, \quad (20)$$

$$n_{\text{eff}}(\lambda) = 2.46 - 1.09(\lambda - \lambda_0) - 0.038(\lambda - \lambda_0)^2. \quad (21)$$

To evaluate the impact of fabrication variations on interferometric performance, we compute the free spectral range (FSR) using Equation 14, where $\lambda = 1550 \text{ nm}$ is the design central wavelength. Using the group indices obtained from the corner analysis in Lumerical MODE, we calculate the expected range of FSR values for various ΔL values, shown in Table 4. We observe that as ΔL increases, the FSR decreases, consistent with theoretical expectations. Additionally, variations in group index cause fluctuations in the FSR of up to 1.5 nm for a given ΔL .

Figure 8 shows the effective and group index for all four corners as a function of wavelength.

Layout

The initial devices were designed using KLayout software. The final design layout is shown in Figure 9.

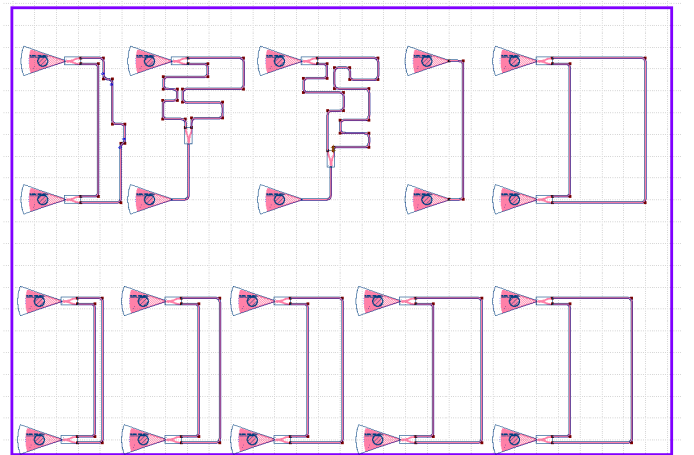


Figure 9: Final proposal of MZI devices in KLayout software.

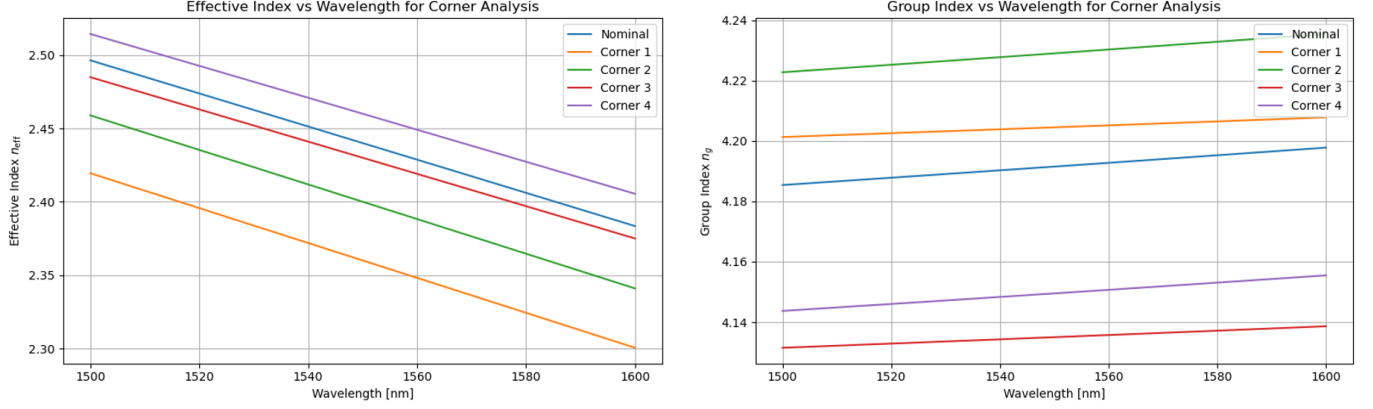


Figure 8: Left: Corner analysis of effective index as a function of wavelength. Right: Corner analysis of group index as a function of wavelength. Both for strip waveguide width of 500nm and a height of 220 nm.

ΔL (μm)	FSR (Corner 1)	FSR (Corner 2)	FSR (Corner 3)	FSR (Corner 4)
25	22.7	22.1	24.1	23.0
50	11.3	11.1	12.0	11.5
75	7.6	7.4	8.0	7.7
100	5.7	5.5	6.0	5.7
125	4.5	4.4	4.8	4.6
150	3.8	3.7	4.0	3.8

Table 4: FSR (in nm) calculated from corner group indices for various ΔL values.

The proposal includes 10 TE MZI devices, each varying in ΔL . Each device is designed according to SiEPIC's internal verification processes, including functional layout checks and KLayout design rule checks. MZI's 7, 8, and 9 (top right in Figure 9) are designed to test how waveguide variability affects the group index calculation and measurement results.

Fabrication

The photonic devices outlined in this report were fabricated through a NanoSOI multi-project wafer (MPW) process by Applied Nanotools Inc. in Edmonton, Canada. Fabrication is based on direct-write 100 keV electron beam lithography using a JEOL JBX-8100FS system at the University of British Columbia. The devices were fabricated on 200 mm diameter silicon-on-insulator (SOI) wafers with a 220 nm silicon device layer and a 2 μm buried oxide (BOX). Wafers were diced into 25 mm \times 25 mm substrates and cleaned with piranha solution (3:1 $\text{H}_2\text{SO}_4\text{:H}_2\text{O}_2$). Hydrogen silsesquioxane (HSQ) resist was spin-coated, baked, and exposed. Proximity effect correction and optimized shape writing were used during exposure. After development in tetramethylammonium sulfate (TMAH), an anisotropic chlorine-based ICP-RIE etch was performed. Following etching, HSQ removal was completed using

a buffered oxide etch. Pattern fidelity was verified using scanning electron microscopy (SEM). Finally, a 2.2 μm silicon dioxide cladding was deposited using plasma-enhanced chemical vapor deposition (PECVD) with a TEOS precursor.

Measurement Description

To characterize the devices, a custom-built automated test setup [6] [7] with automated control software written in Python was used [8]. An Agilent 81600B tunable laser was used as the input source and Agilent 81635A optical power sensors as the output detectors. The wavelength was swept from 1500 to 1600 nm in 10 pm steps. A polarization maintaining (PM) fibre was used to maintain the polarization state of the light, to couple the TE polarization into the grating couplers [9]. A 90° rotation was used to inject light into the TM grating couplers [9]. A polarization maintaining fibre array was used to couple light in/out of the chip [10].

Measurement Data Analysis

The experimental data for the 10 TE-polarized devices shown in Figure 9 will be analyzed in this section. However, only a detailed data analysis process will be provided for 2 MZIs. This procedure involved applying a baseline correction to the data to remove the baseline shape of the grating couplers. To flatten the spectrum, we apply a low-order polynomial fit, and subtract this from the data.

A on-chip loopback calibration structure was used to account for the interferometric response of the MZIs. This structure consists of two grating couplers connected by a single waveguide segment of 150 μm . Through this calibration we are able to account for insertion loss of the grating couplers and the waveguide propagation loss. The loopback structure provides a reference which is subtracted from the measured MZI spectrum, which ensures the group index only depends on the intrinsic fringes of the MZI. To do this, a polynomial is fit to the loopback response, and the baseline is subtracted from the MZI spectra to mitigate the insertion loss. Figure 10 shows the insertion loss of the loopback structure.

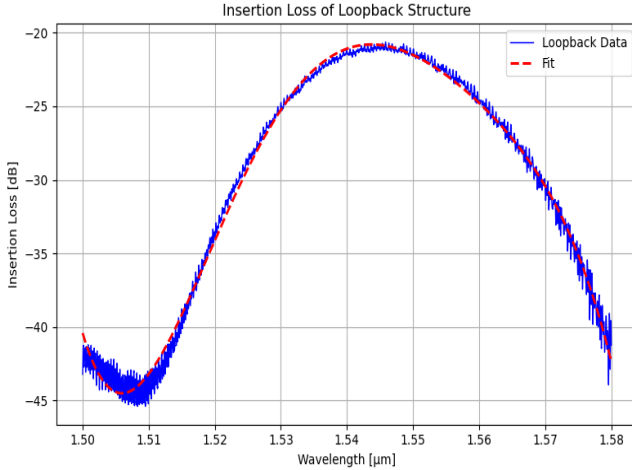


Figure 10: Insertion loss of loopback calibration structure.

The group index of the waveguides was extracted through the least-squares curve fitting method. The resulting spectrum fit for MZI 4 ($\Delta L = 100\mu\text{m}$) is shown in Figure 11.

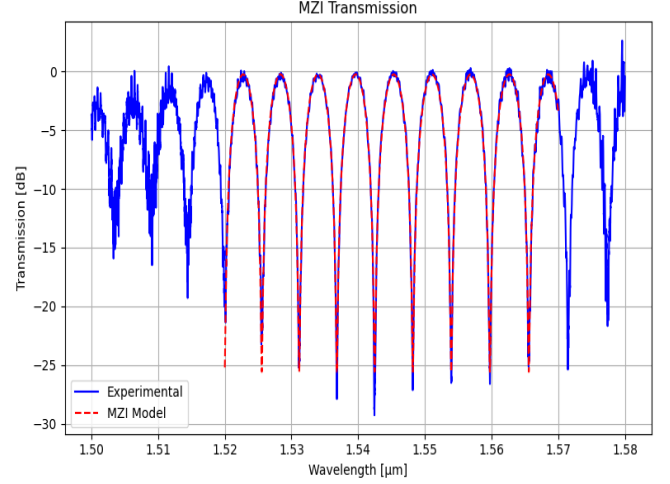


Figure 11: MZI transmission spectrum for MZI 4 ($\Delta L = 100\mu\text{m}$).

Once the experimental data was fit using the least squares method, the group index was extracted using the derivative of the effective index with respect to wavelength. To do this, the effective index as a function of wavelength was modelled as a second-order polynomial (Equation 17) and the derivative $\frac{dn_{eff}}{d\lambda}$ was evaluated to compute Equation 1. We see the extracted group index resides within the corner values for $\Delta L = 100\mu\text{m}$ in Figure 12.

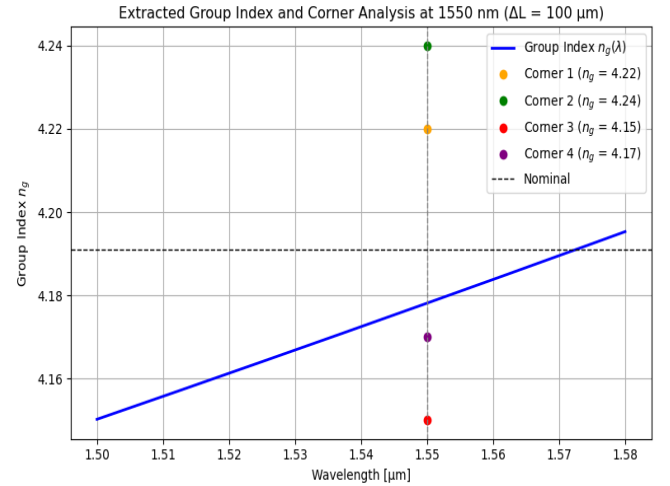


Figure 12: Extracted group index as a function of wavelength, with corresponding corner analysis values at $\lambda = 1550\text{nm}$.

We can also look at the results for MZI 5 ($\Delta L = 125\mu\text{m}$). Figure 13 (a) and (b) shows the MZI transmission and the extracted group index. We see the estimated group index at 1550nm for MZI 5 also falls within the corners. A summary of the extracted group indices and the relative error to the nominal value is shown in Table 5. We see all the devices are within reasonable error to the nominal simulated

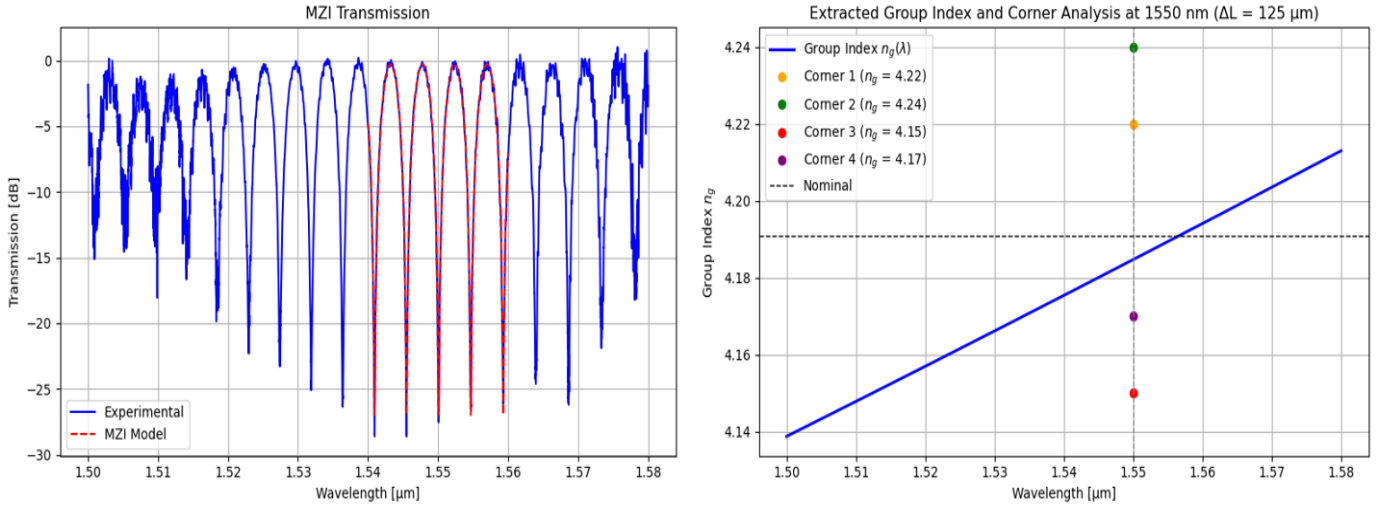


Figure 13: Left: Transmission spectrum of MZI with $\Delta L=125 \mu\text{m}$. Right: Extracted group index with corner values.

n_g for a strip waveguide of 220nm and width of 500nm, and only one extracted group index is not within the corners. MZI 1, with a $\Delta L = 25\mu\text{m}$, has a 9.56% error to the nominal simulated group index. This large deviation is due to the interference fringes in the transmission spectrum being extremely close together. The high fringe density as a function of wavelength makes the spectrum difficult to fit with a least squares approximation. This device is a clear anomaly, as no channels showed clear interference fringes to analyze.

We also see for MZIs 7, 8, and 9 (devices with bends), the deviation from the nominal value remains relatively static. This is interesting, as the devices were included out of curiosity to see the affect that waveguide bends have on the group index estimation. We see MZI 6 and MZI 9 ($\Delta L=150 \mu\text{m}$) both achieve the identical deviations from the nominal value, even though MZI 9 a significantly more curved layout.

Device	$\Delta L (\mu\text{m})$	Extracted n_g	Error
MZI 1	25	3.790	-9.56%
MZI 2	50	4.176	-0.36%
MZI 3	75	4.180	-0.26%
MZI 4	100	4.178	-0.31%
MZI 5	125	4.184	-0.17%
MZI 6	150	4.181	-0.24%
MZI 7	50	4.261	+1.67%
MZI 8	75	4.171	-0.48%
MZI 9	150	4.181	-0.24%
MZI 10	Loopback	n/a	n/a

Table 5: Percentage error of extracted group index values relative to nominal simulated value $n_g = 4.191$.

Acknowledgments

I acknowledge the edX UBCx Phot1x Silicon Photonics Design, Fabrication and Data Analysis course, which is supported by the Natural Sciences and Engineering Research Council of Canada (NSERC) Silicon Electronic-Photonic Integrated Circuits (SiEPIC) Program. The devices were fabricated by Richard Bojko at the University of Washington Washington Nanofabrication Facility, part of the National Science Foundation's National Nanotechnology Infrastructure Network (NNIN), and Cameron Horvath at Applied Nanotools, Inc. Omid Esmaeeli performed the measurements at The University of British Columbia. We acknowledge Lumerical Solutions, Inc., Mathworks, Mentor Graphics, Python, and KLayout for the design software.

References

- [1] Xuetong Zhou et al. "Silicon photonics for high-speed communications and photonic signal processing". In: *npj Nanophotonics* 1.1 (July 2024), p. 27. ISSN: 2948-216X. DOI: 10.1038/s44310-024-00024-7. URL: <https://doi.org/10.1038/s44310-024-00024-7>.
- [2] Yaocheng Shi et al. "Silicon photonics for high-capacity data communications". In: *Photon. Res.* 10.9 (Sept. 2022), A106–A134. DOI: 10.1364/PRJ.456772. URL: <https://opg.optica.org/prj/abstract.cfm?URI=prj-10-9-A106>.
- [3] Shihan Hong et al. "Versatile parallel signal processing with a scalable silicon photonic chip". In: *Nature Communications* 16.1 (2025), p. 288. ISSN: 2041-1723. DOI: 10.1038/s41467-

024 - 55162 - 5. URL: <https://doi.org/10.1038/s41467-024-55162-5>.

- [4] Lantian Feng et al. "Silicon photonic devices for scalable quantum information applications". In: *Photon. Res.* 10.10 (Oct. 2022), A135–A153. DOI: 10.1364/PRJ.464808. URL: <https://opg.optica.org/prj/abstract.cfm?URI=prj-10-10-A135>.
- [5] Graham T. Reed and Andrew P. Knights. *Silicon Photonics: An Introduction*. Chichester, UK: John Wiley & Sons, 2004.
- [6] Lukas Chrostowski and Michael Hochberg. *Silicon Photonics Design: From Devices to Systems*. Cambridge University Press, 2015. Chap. 12.
- [7] Maple Leaf Photonics. *Company Website*. <http://mapleleafphotonics.com>. Seattle, WA, USA; Accessed: 2025-06-25.
- [8] Michael Caverley. *SiEPIC Probe Station Software*. <http://siepic.ubc.ca/probestation>. Accessed: 2025-06-25.
- [9] Yun Wang et al. "Focusing sub-wavelength grating couplers with low back reflections for rapid prototyping of silicon photonic circuits". In: *Optics Express* 22.17 (2014), pp. 20652–20662. DOI: 10.1364/OE.22.020652.
- [10] PLC Connections. *Company Website*. <http://www.plcconnections.com>. Columbus, OH, USA; Accessed: 2025-06-25.